Contents lists available at ScienceDirect

Nuclear Materials and Energy

journal homepage: www.elsevier.com/locate/nme

Parameter dependencies of the experimental nitrogen concentration required for detachment on ASDEX Upgrade and JET

S.S. Henderson [a], M. Bernert [b], C. Giroud [a], D. Brida [b], M. Cavedon [b], P. David [b], R. Dux [b], J. R. Harrison [a], A. Huber [c], A. Kallenbach [b], J. Karhunen [e], B. Lomanowski [d], G. Matthews [a], A. Meigs [a], R.A. Pitts [f], F. Reimold [g], M.L. Reinke [d], S. Silburn [a], N. Vianello [h], S. Wiesen [c], M. Wischmeier [b], the EUROfusion MST1 team[1], ASDEX Upgrade team[2], JET contributors[3]

[a] UKAEA, CCFE, Culham Science Centre, Abingdon OX14 3DB, UK
[b] Max-Plank-Institut für Plasmaphysik, D-85748 Garching, Germany
[c] Forschungszentrum Jülich GmbH, Institut für Energie-und Klimaforschung, 52425 Jülich, Germany
[d] Oak Ridge National Laboratory, Oak Ridge, TN 37831, USA
[e] Aalto University, Department of Applied Physics, 02150 Espoo, Finland
[f] ITER Organization, Route de Vinon-sur-Verdon, CS 90 046, 13067 St. Paul Lez Durance Cedex, France
[g] Max-Plank-Institut für Plasmaphysik, 17489 Greifswald, Germany
[h] Consorzio RFX (CNR, ENEA, INFN, Universita di Padova), Corso Stati Uniti 4, 35127 Padova, Italy

ABSTRACT

While current tokamak experiments are beginning to use real-time feedback control systems to manage the plasma exhaust, future tokamaks still require validation of theoretical models used to predict the threshold impurity concentration required to sufficiently reduce the power and particle fluxes to the divertor. This work exploits new spectroscopic measurements of the divertor nitrogen concentration, c_N, in partially detached N_2-seeded H-mode plasmas on ASDEX Upgrade (AUG) and JET with the ITER-Like Wall (JET-ILW) to test the parameter dependencies of the power flowing to the outer divertor, $P_{div,outer}$, and the separatrix electron density, $n_{e,sep}$. A least-squares regression of the AUG measurements demonstrates that the threshold c_N required for detachment scales as $c_N \propto P_{div,outer}^{1.19 \pm 0.32} n_{e,sep}^{-2.77 \pm 0.36}$. This scaling of $n_{e,sep}$ is also consistent with the measurements from JET which, at constant $P_{div,outer}$, show $c_N \propto n_{e,sep}^{-2.43 \pm 0.27}$. The dependencies of $P_{div,outer}$ and $n_{e,sep}$ is demonstrated over at least a factor of two change in both parameters and indicates a stronger dependence on $n_{e,sep}$ in comparison to the Lengyel model, which could be due to the assumption in this model that the heat flux channel width is independent of density. This first assessment of detachment scaling with impurity seeding highlights the need for further analysis of the systematic uncertainties of the measurement and more consistent scenarios from more tokamaks to investigate the machine size scaling.

1. Introduction

Reducing power and particle fluxes impacting on the divertor targets is one of the key challenges facing future fusion experiments. One way to achieve this is through substantial seeding of impurities, such as N_2, Ne, or Ar, which will be used on ITER to facilitate stationary operation with acceptable power and particle fluxes to the divertor [1]. Despite impurity seeding being used for many years and on many different tokamaks

[2–9], direct measurements of the seeding gas concentration are limited [10,11]. Current tokamaks have developed real-time feedback systems to control the divertor detachment state (e.g. measuring the outer divertor temperature using Thomson scattering or shunt current measurements [12,13]) and the radiation inside the separatrix (e.g. with AXUV diodes measuring the X-point radiation location [14]). These systems do not require any detailed knowledge of the impurity concentration. However, the successful design of future tokamaks rely on

validated predictions of the impurity concentration to ensure an integrated scenario compatible with both the core and edge plasma.

Attempts to predict the impurity concentration have been made using sophisticated scrape-off layer (SOL) simulation codes, such as SOLPS [1,15], and by using simpler approximations derived from the Lengyel model [16–21]. Validating the predicted impurity concentrations from these models in current devices is therefore of high importance and, recently, a method was developed to measure the N concentration, c_N, in the outer divertor of ASDEX Upgrade (AUG) using a new spectroscopic N II line ratio technique [22,23]. The divertor spectrometer setup required to measure the c_N is standard on both AUG and JET-ILW which made it possible to scan a wide range of shots to find N_2 seeded H-mode plasma scenarios with a partially detached outer divertor (and steady upstream SOL conditions) to assess the c_N measurements. From this database, this paper presents the first experimental assessment of c_N in two, metal-walled tokamaks with vertical outer divertor configurations to demonstrate the key parameter dependencies to reach detachment, including the scaling with the separatrix density $n_{e,sep}$ and the power flowing to the outer divertor $P_{div,outer}$.

The paper is structured as follows: Section 2 and 3 present the range of SOL parameters assessed in the database and an overview of the model used to measure c_N. The parameter dependencies from the database are analysed using a least-squares regression in Section 4. Comparison of the measurements to theoretical scaling laws, which include the Lengyel approach or its close equivalent, are presented in Section 5. Concluding remarks are given in Section 6.

2. Experimental database

The database used to assess the threshold c_N required to reach detachment spans 13 pulses on AUG and 9 pulses on JET-ILW. Each pulse has a phase of N_2 seeding during H-mode with a partially detached outer divertor. The detachment state of the outer divertor is assessed on AUG by using the real-time estimate of the outer divertor temperature, T_{div}, derived from shunt measurements and scaled to approximately match the outer strike-point temperature [24,13]. On JET, both the roll-over of the ion saturation current and temperature estimate from Langmuir probe (LP) measurements in the outer divertor are used to estimate the detachment state [7]. Furthermore, since simulations show that the N II emission front is a good indicator for the poloidal location of the deuterium ionisation front [25], a combination of N II measurements from spectroscopy and filtered divertor camera images are used to verify the LP measurements on JET. The c_N used in this analysis are those

measured when the outer divertor is partially detached, where there is significant reduction of the heat flux and pressure between the midplane and divertor target within the first power decay length in the SOL. On AUG, this approximately corresponds to $T_{div} = 3 - 5$ eV. The parameter dependencies discussed in Section 4 may be different if deeper detachment is required; i.e. 'pronounced' or 'full' detachment using the level descriptor parlance defined in [26], where there is significant heat flux and pressure reduction over several power widths.

While the detachment state on JET can be assessed self-consistently, the lack of an equivalent T_{div} measurement will introduce an uncertainty when comparing to AUG. It is shown later in Section 4.1 that a change in T_{div} of a few eV can change the required c_N by 10 − 20%.

The spectrometer sightlines used to determine the concentrations are vertically viewing on JET and horizontally viewing on AUG, as shown in Fig. 1. However, the N II emission in the SOL is typically localised close to the separatrix, as shown in Fig. 2, and therefore differences in interpretation due to line-integration are negligible. Lastly, the database between JET and AUG have not been optimised to produce similarity experiments [27]; however, on both machines, the outer divertor target is located on the vertical target as shown in Fig. 1.

The database includes a range of parameters as described in Table 1. P_{sep}, the power crossing the separatrix, is defined as $P_{sep} = P_{input} - P_{rad,main} - dW/dT$, where P_{input} is the total input power, $P_{rad,main}$ is the radiated power measured by bolometry in the main chamber volume, and W is the plasma stored energy. The $n_{e,sep}/n_{GW}$ fractions are $0.2 - 0.3$ and $0.3 - 0.4$ on AUG and JET, respectively, while the line averaged core densities on both machines are $7 - 10 \times 10^{19}$ m^{-3}. On AUG, only 1 pulse in the database had $B_T = 1.9$ T while the remaining pulses were ≈ 2.5 T. Therefore, B_T was not considered in the scaling.

3. Divertor nitrogen concentration

The line-integrated N II radiance measurement from a line of sight passing through the outer divertor leg is used infer the fraction of nitrogen over deuterium ions, c_N, using the following equation

$$c_N = \frac{4\pi I_{NII}}{(f_{N^+} PEC^{exc} + f_{N^{2+}} PEC^{rec})} \frac{1}{\Delta L n_{e,NII}^2}, \tag{1}$$

where I_{NII} is the absolutely calibrated N II radiance in $[ph/s/m^2/steradian]$, ΔL is the length of the N II emitting region through the line-of-sight (LOS) in $[m]$, $PEC^{exc,rec}$ are excitation and recombination photon emissivity coefficients [22] in $[m^3/s]$, f_{N^z} is the fractional
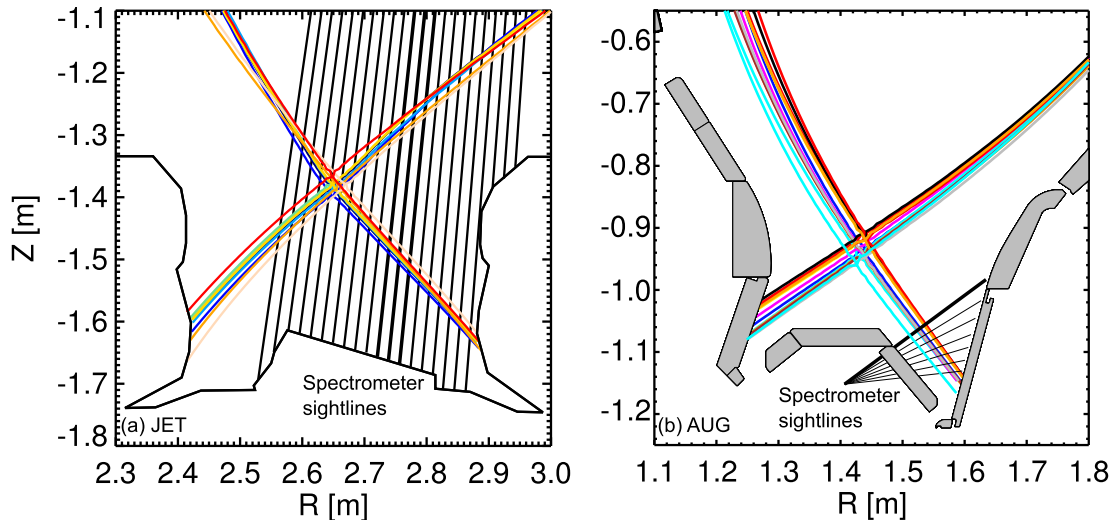

Fig. 1. The last closed flux surface is shown for each shot used in the database. Divertor spectrometer sightlines on both (a) JET and (b) AUG are shown for reference, where the LOS for JET are the KT3B lines shown in Fig. 2.
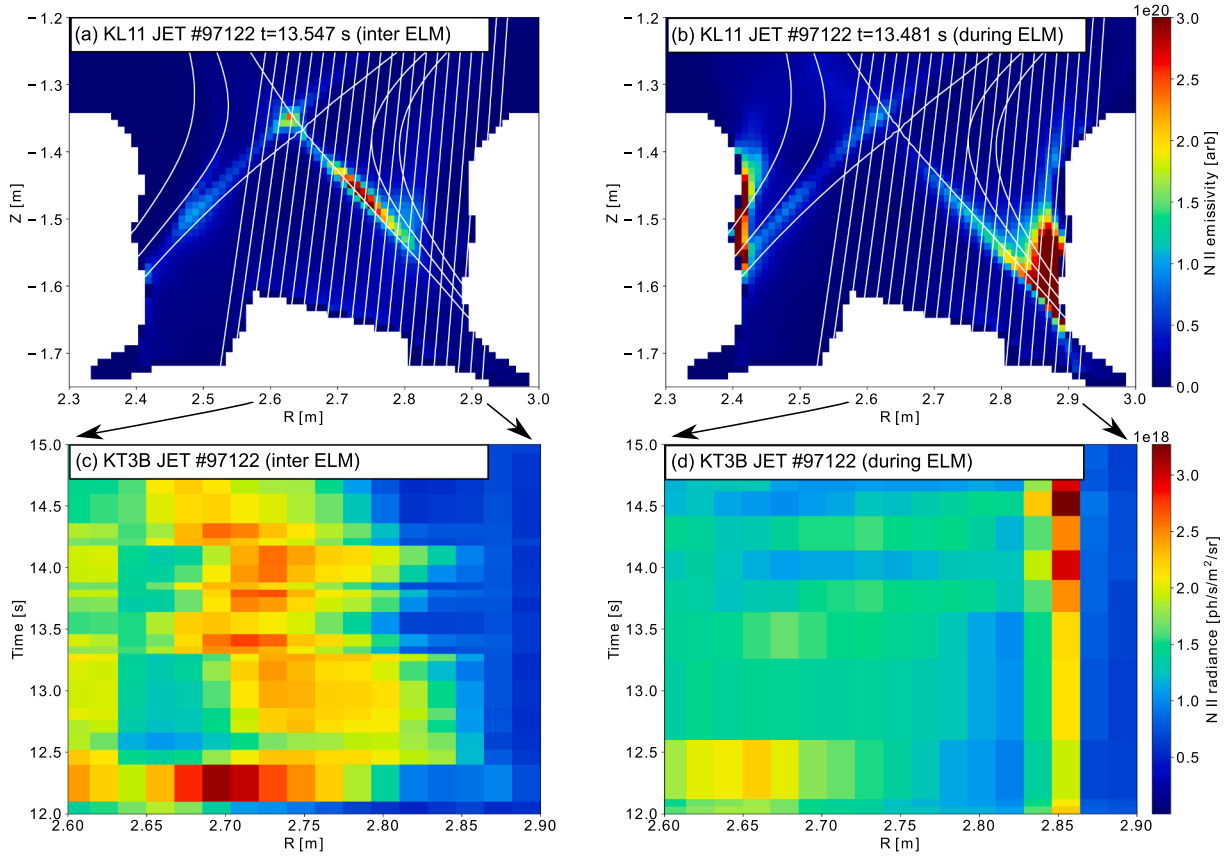
Fig. 2. Tomographic inversions of the divertor camera images on JET (KL11), filtered to the narrow band-pass covering the N II emission at $\lambda = 500.4$ nm are shown for (a) an inter-ELM time frame and (b) a time frame that integrates over the whole ELM peak during JET #97122. Note that the same colour scale is used in both (a) and (b) and has been artificially saturated to demonstrate the differences in poloidal location of the emission. The radiance of the N II line at $\lambda = 404.1$ nm from the divertor spectrometer measurements (KT3B) in the same pulse fitted during inter-ELM and ELM time windows is shown in (c) and (d), respectively.

Table 1
Range of parameters within the database.

Parameter	AUG	JET
$n_{e,sep}$ [10^{19} m^{-3}]	$2-4$	$2.2-3.5$
P_{sep} [MW]	$3.5-12$	$14-15.5$
B_T [T]	$1.9-2.5$	2.7
q_{95}	$4-5$	3
I_P [MA]	$0.8-1.2$	2.5
κ	1.7	1.7
a_{min}	0.5	0.9

ion abundance of the Z charged ion (e.g. N$^+$ for N II radiance) and $n_{e,NII}$ is the electron density in [m^{-3}] averaged through the LOS. The f_{N^Z} is calculated using a zero-transport ionisation balance. The assumption of zero-transport was tested in Fig. 7 of [22] and shown to be valid for temperatures measured below ≈ 4 eV. This is also discussed further in Section 3.2. The impact of emission driven by charge exchange has not yet been considered.

3.1. Impact of ELMs

The principal spectrometers used on AUG and JET are the Czerny Turner-like visible spectrometer [28] and the mirror-linked spectrometer [29], which have temporal resolutions of 400 Hz and 25 Hz, respectively. The sightline geometries for the JET and AUG spectrometers are shown in Fig. 1.

In the shots included in the database, the ELM frequency on AUG is

typically greater than ≈ 100 Hz, while on JET they range from $25-100$ Hz. Where inter ELM measurements are not possible, it is crucial to assess the impact of the ELM on the N II radiance measurement, in particular for spectroscopy on JET where the integration time is typically longer than the time between ELMs. Tomographic reconstructions of the filtered divertor camera images measured on JET [30], which account for reflections, are used to assess the impact of ELMs in JET #97122 which has a sufficiently low ELM frequency (≈ 25 Hz) and a partially detached outer target. The camera has a temporal resolution of 62.5 Hz and an exposure time of 3 ms. The inverted N II emission measured inter-ELM and during the ELM is shown in Fig. 2a and b, respectively, where the same colour scale is used in both.

During the inter-ELM phase, the peak N II emission is located midway between the X-point and strike-point close to the separatrix. When the ELM occurs, the N II emission in this region decreases, and the emission next to the strike-point increases significantly, likely because the temperature along the SOL rises during the ELM. The N II radiance measured by the spectrometer during inter- and intra-ELM periods is shown in Fig. 2c and d, respectively. Consistent with the inverted camera images, the N II radiance between $2.6 < R < 2.8$ m is approximately 50% dimmer during the ELM, in comparison to the inter-ELM phase, where R is the major radius defined where the spectrometer LOS intercept the horizontal divertor target plate. Similarly, the N II radiance between $2.8 < R < 2.85$ m is significantly brighter during the ELM.

Using the spectrometer LOS geometry to integrate the N II emission from the inverted camera data to produce equivalent measurements to the spectrometer, the impact of ELMs can be assessed at higher temporal resolution. The line-integrated inverted camera data taken along the $R =$

2.85 m and $R = 2.7$ m sightlines is shown in Fig. 3, with the ELM time subtracted from the time base. Around 10 ms after the ELM, the N II radiance at $R = 2.7$ m decreases by $\approx 50\%$ and then recovers to the pre-ELM radiance by 20 ms. On AUG, it was similarly shown [22] that ELMs decrease the intensity of the N II radiance measured through the AUG sightline shown in bold in Fig. 1b; however, the decrease was less ($\approx 20\%$). Like JET, the N II radiance measured through the LOS viewing closer to the strike-point on AUG is significantly increased during the ELM.

While the drop in radiance appears to be more severe on JET, the longer spectrometer integration time (40 ms) produces an averaged intra- and inter- ELM radiance, which is weighted more to the inter-ELM value. This reduces the overall decrease on the measurement produced by the ELM to $\approx 20\%$. Additionally, caution should be taken when using this technique to measure the c_N in scenarios with ELM frequencies > 100 Hz on JET, as there would be no stationary inter-ELM phase.

Therefore, on both machines, inter-ELM line-integrated radiance measurements are used wherever possible, with the sightline on AUG shown in bold in Fig. 1b and on JET from sightlines $R < 2.8$ m. However, in discharges where inter-ELM data is not available (because the ELM frequency is too high) the c_N will likely be under-estimated by up to 20%.

3.2. Temperature and density

The c_N measurement is dependent on the temperature and density of the plasma associated with the N II emission, referred to as $T_{e,NII}$ and $n_{e,NII}$, respectively. The $T_{e,NII}$ and $n_{e,NII}$ drive the rate of excitation and recombination, while from Eq. 1 $c_N \propto 1/n_{e,NII}^2$. Measurements of the two spectroscopic line ratios used to determine $T_{e,NII}$ and $n_{e,NII}$ [22] are shown in Fig. 4; the time windows are limited on AUG to $T_{div} = 0 - 20$ eV (i.e. using the T_{div} shunt measurement specific to AUG) and on JET to $t - t_{seed} = 1 - 2.5$ s, where t_{seed} is the time where the seeding begins. The scatter of measured line ratios on both JET and AUG falls between contours of constant temperature between $2 - 4.5$ eV. The temperatures close to 2 eV are mostly measured in sight lines viewing close to the strike-point. The average line ratios, shown by the crosses in Fig. 4a and b, fall between $3 - 4$ eV. The difference in viewing geometry between AUG and JET can explain the modest changes in average n_e and T_e found between the sightlines.

When multiplying the atomic excitation and recombination emission coefficients by the fractional abundance of the N^+ and N^{2+}, respectively, the N II emission is predicted to peak at ≈ 3.5 eV, consistent with the
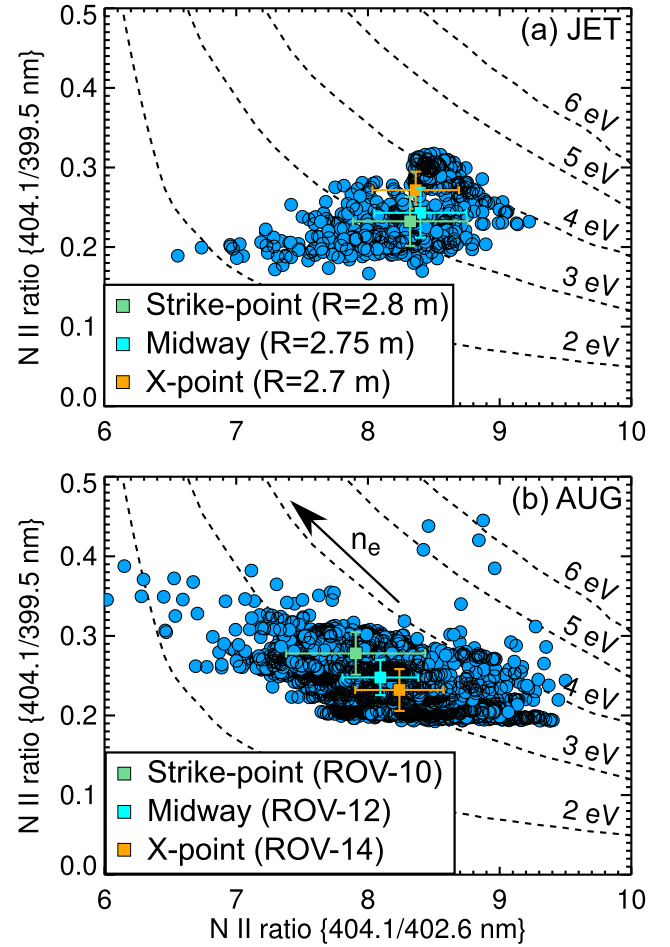
Fig. 4. N II line ratios for all shots in the database for (a) JET measured between $t - t_{seed} = 1 - 2.5$ s and (b) AUG measured between $T_{div} = 0 - 20$ eV. The average ratios for each sightline are shown by the square symbols. Contours of T_e calculated using the atomic rate coefficients are shown by dashed lines, with n_e increasing from right to left in each figure.

averaged $T_{e,NII}$ measurements shown in Fig. 4. Furthermore, it has been previously demonstrated (e.g. Fig. 7 in [22]) that $T_{e,NII}$ measurements of ≤ 4 eV can be reliably measured independent of whether transport is significantly changing the ionisation balance.

3.3. Length of emission

The values of c_N discussed in this paper assume that line-integration effects are negligible, and that the N II emission originates from a narrow, localised layer of plasma of constant T_e and n_e intercepting the spectrometer LOS. Furthermore, as described in Eq. 1, the model assumes that this thin layer of plasma can be simply described by a unit length (i.e. $c_N \propto 1/\Delta L$). In the divertor configurations considered in this analysis, the N II emission between the X-point and the poloidal (upstream) location of the N II front is typically localised to a thin layer spread across the private flux region (PFR) and separatrix, as shown in Fig. 2a. However, due to the uncertainty in the equilibrium and inverted data, any distinction of the location between SOL and PFR should be treated cautiously. Conversely, the N II emission between the front and the strike-point in Fig. 2a shows a weaker, but still significant, cloud of emission spread across the SOL. Therefore, due to the localisation of the measurement, only spectroscopic measurements between the front location and the X-point are used to infer c_N.

The emission profile through a divertor spectrometer LOS on JET, calculated using the data from the inverted camera image, is shown in
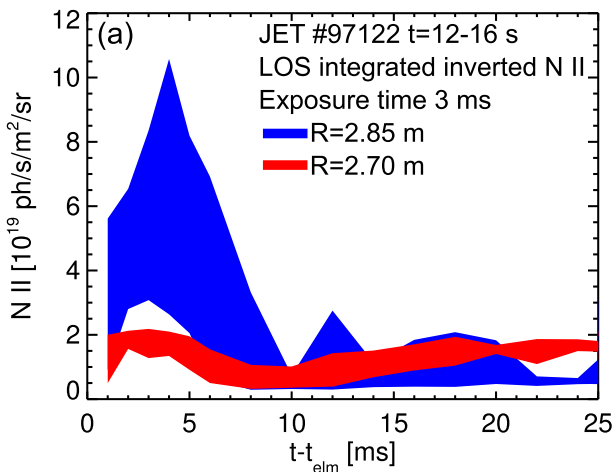
Fig. 3. The N II emission from the inverted camera images, line integrated along the divertor spectrometer sightlines at R = 2.85 m and R = 2.7 m, is shown as a function of ELM time, $t - t_{ELM}$, for JET #97122. The camera data is measured with a temporal resolution of 62.5 Hz and an exposure time of 3 ms.
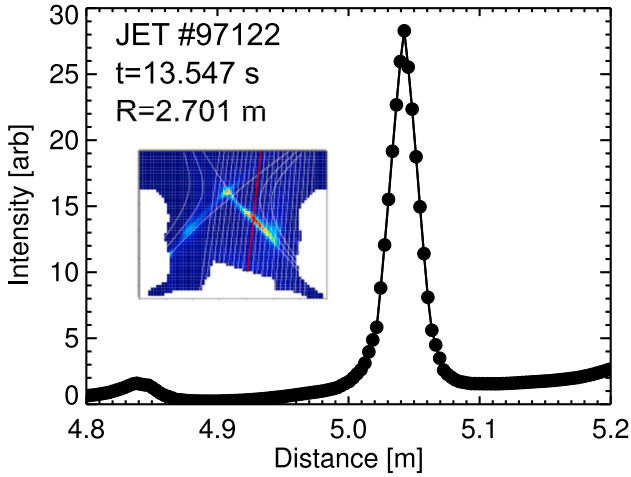
Fig. 5. N II emission from a inverted divertor camera image shown as a function of the distance along the divertor spectrometer channel measuring at R = 2.70 m for JET #97122 at t = 13.547 s.

Fig. 5. For JET, $\Delta L = 7$ cm produces an intensity that is $\approx 70-75\%$ of the peak value of the inverted data shown along the sightline in the outer divertor. The moderate over-estimation of ΔL on JET is to account for any weaker radiation from the SOL region above the X-point measured due to the vertical viewing geometry and also due to reflections which are expected to increase the N II emission by $< 15\%$ on JET [30]. For each time step, the front location is calculated by finding the peak N II radiance measured by the divertor spectrometer across the radius (within $R \le 2.8$ m). ΔL is reduced to 5 cm in LOS measuring further upstream towards the X-point.

Although the equivalent inverted images of N II are not available on AUG, the emission is expected to be localised close to the separatrix as found in SOLPS modelling [15]. ΔL is modelled as a function of T_{div} on AUG, as described in [22]. It is possible that ΔL could vary with the PFR spreading factor S. In L-mode, S has been shown to scale approximately as $1/I_P$ [31], but this scaling has not yet been verified in H-mode. As there is no clear model to describe how ΔL should vary with I_P, it is calibrated at 6 cm on AUG for $T_{div} = 3-5$ eV which is consistent with a coarse inversion of the N II radiances measured using the full set of divertor sightlines. However, using the L-mode scaling and assuming ΔL scales linearly with S, values of $\Delta L = 7.5, 6.0, 4.5$ cm would account for $I_P = 0.8, 1.0, 1.2$ MA, respectively. The potential impact of this is discussed in Section 4. On JET, I_P remains constant. The systematic uncertainty of ΔL is therefore expected to be of the order ± 1.5 cm.

3.4. Concentration measurements and uncertainties

The spectrometer sightlines on both AUG and JET allow for c_N measurements localised along the separatrix in the outer divertor. It is more convenient to use one representative c_N for the outer divertor in each shot when assessing the threshold c_N for detachment. Therefore, the radial c_N measurements on JET are averaged over three radial channels between the front location and the X-point; these three channels change as the front position moves, but in practice mostly the same channels (shown in bold in Fig. 1a) are used since the detachment state has been kept consistent within the database. On AUG, as discussed in the sections above, only one LOS channel (bold line in Fig. 1b) is used to represent the outer divertor c_N as the spatial resolution is lower than JET. The c_N are then averaged on AUG over all time slices where the SOL conditions are steady and $T_{div} = 3-5$ eV, while on JET they are averaged over $t - t_{seed} = 1-2.5$ s where the camera inversions and probe measurements indicate partially detached divertor conditions equivalent to $T_{div} = 3-5$ eV on AUG.

There are two main sources of uncertainty in the measured c_N: the

$T_{e,NII}$ and $n_{e,NII}$ predicted from line ratios and the ΔL model. The impact of reflections from the metal wall is less significant on AUG as the spectrometer LOS end in viewing dumps.

The uncertainty of $T_{e,NII}$ and $n_{e,NII}$ is caused by the quality of the spectral fits: the quality of the atomic data is discussed in [22]. On AUG, the typical errors on the 404.1/399.5 nm and 404.1/402.6 nm N II line ratios, called LR1 and LR2, are $\approx 1\%$ and $\approx 2\%$, respectively. This propagates to an uncertainty of $\approx 10\%$ on $T_{e,NII}$ and $n_{e,NII}$, which subsequently produces an overall c_N uncertainty of $\approx 20-30\%$. Furthermore, in pulses with low N_2 seeding, the N II line at $\lambda = 402.6$ nm is two orders of magnitude weaker than the $\lambda = 399.5$ nm N II line and is often blended with another line (thought to be from F II). In these scenarios, the $T_{e,NII}$ is approximated to be $3.1-3.5$ eV which can lead to higher c_N uncertainties of $30-40\%$, where the errors have been added in quadrature. Overall, these uncertainties outweigh those from the ΔL model.

LR1 and LR2 have significantly lower uncertainties from JET measurements ($\le 0.3\%$) and generate a modest uncertainty of $\approx 5\%$ on c_N. This is mainly due to better statistics on the measured spectral radiance (because of the longer integration time of the spectrometer). Therefore, the leading uncertainty on JET is driven by the averaging of c_N over the three radial channels and over the time window of constant partially detached divertor conditions ($1-2.5$ s). The change in measurement between the radial channels is likely due to small changes in ΔL that are not accurately reflected in the modelled ΔL.

The uncertainty associated with the absolute calibration of the diagnostic and window transmission is assumed negligible here in comparison to the leading order uncertainties described above.

Finally, the measured c_N from JET and AUG can be compared to estimates of c_N based on the ratios of the gas valve fluxes,

$$c_{N,flux} = \frac{\Gamma_{N2}/7}{(\Gamma_{D2} + \Gamma_{N2}/7)} \tag{2}$$

where Γ_{N2} and Γ_{D2} are the impurity and main ion gas valve fluxes. Since the valve fluxes are calibrated in electrons/s, the factor 7 on the numerator and denominator converts the flux to atom/s. On AUG, assuming equal pumping speeds for D_2 and N_2, the pumped fluxes in the divertor must correspond to the input gas valve fluxes and therefore the $c_{N,flux}$ would approximately represent the maximum c_N achievable in the divertor. However, while the D_2 pumping speed is known from calibrations [32], the pumping speed for N_2 is the main uncertainty in this model [33]. Furthermore, potential wall sticking/release may result in a lower spectroscopic measurement [34].

Comparisons of the two measurements are shown in Fig. 6 as a function of the intrinsic nitrogen content in the machine which is
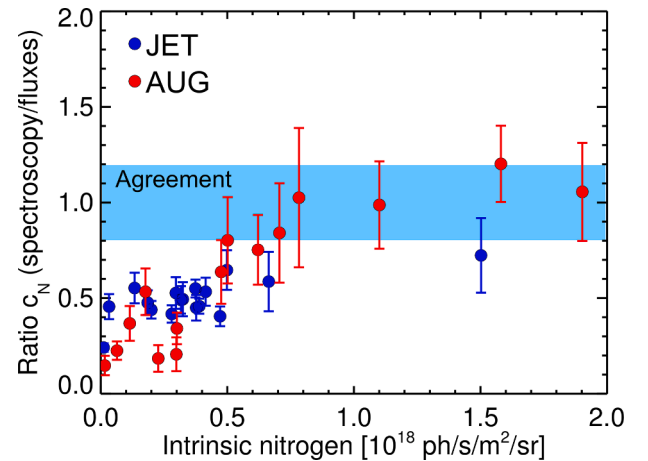

Fig. 6. The ratio of c_N measured from spectroscopy and valve fluxes is shown as a function of intrinsic nitrogen, estimated by using the N II radiance measured immediately before seeding.
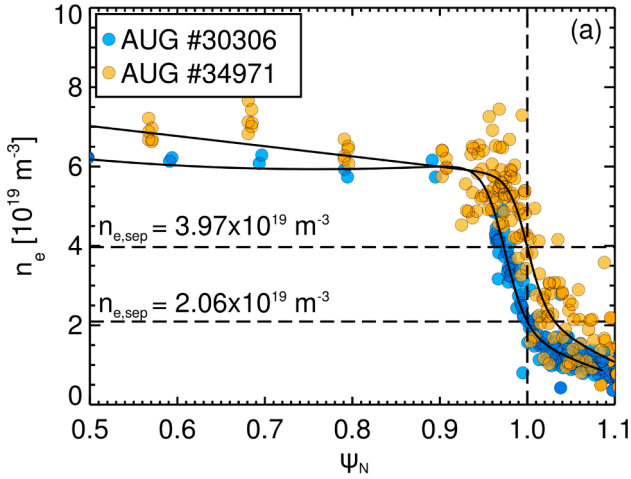
Fig. 7. Fits of inter-ELM n_e from Thomson scattering and Li-beam measurements are shown for two AUG shots, #30306 and #34971.

approximated by the N II radiance measured before the seeding valve is opened. The $c_{N,flux}$ measurements are averaged over the same time window as the spectroscopy measurements. In stationary scenarios with high measured intrinsic N II radiance, indicative of fully saturated vessel surfaces, the measurements agree on AUG; however, when the intrinsic N II radiance is low, the two measurements can differ by an order of magnitude.

On JET, a similar but less pronounced trend is found, with ratios remaining around 0.5 in most pulses. The smaller difference in ratios found over the range of intrinsic N II radiance could be due to the seeding recipe used on JET, which typically injects a large amount of N_2 for a short time window at the start of injection, before reducing to the requested amount. This may be an effective technique for rapidly saturating the vessel walls, and therefore ensuring that the N concentration reaches a steady state value that is repeatable in different pulses, regardless of the machine conditions prior to seeding. On AUG, the shots in this database do not have this initial short phase of larger N_2 seeding influx.

4. Parameter dependencies

In principle, any regression analysis should include all parameters that are varying across the database. The choice of parameter dependencies in this analysis, noted in Section 2, have been guided by theoretical scaling laws (see Section 5). Other unknown parameters may be affecting the measured c_N required for detachment; for example, the connection length between X-point and target, the parallel transport, and the divertor closure. While the changes in these parameters across the database are modest, their impact on the derived threshold c_N for detachment cannot be ruled out. In future, the scaling of B_T should also be assessed.

Since this analysis focuses solely on the scaling of detachment in the outer divertor, a fraction of P_{sep} is used in the scaling according to an in-out power asymmetry of $1:2$ and a fraction $1-1/e$ which is lost either to the wall or to the divertor SOL outside the first power width flux tube [18]. This leads to a corrected power entering the outer divertor defined as $P_{div,outer} = P_{sep}/\alpha$ where $\alpha = 1.5/(1-1/e) = 2.37$. On JET, α can be measured by comparing P_{sep} integrated over the duration of a pulse and the corresponding thermocouple tile energies covering the vertical outer divertor tiles. Considering only the pulses used in this database, the measured value is $\alpha = 2.26 \pm 0.12$. For consistency, $\alpha = 2.37$ is used to scale P_{sep} on AUG and JET.

The fits to the inter-ELM n_e profiles across the core plasma radius are shown in Fig. 7a for the two data points providing the highest and lowest $n_{e,sep}$. The fits are shifted to match the separatrix temperature, $T_{e,sep}$,

evaluated from the scaling laws given by [35] using the methodology of [36] which includes N_2 seeded plasmas. The uncertainty in $n_{e,sep}$ is taken, arbitrarily, as the standard deviation of the fit from $\psi_N = 0.995 - 1.005$ to account for the $n_{e,sep}$ gradient steepness near the separatrix. The ψ_N range also allows for an uncertainty in the separatrix position, producing typical uncertainties of ±15 eV on the separatrix temperature.

The c_Ns measured on AUG at $I_P = 0.8$ MA contain the largest number of unique points from 8 separate discharges and a factor x2.0 range of $n_{e,sep}$ and factor x1.75 range of $P_{div,outer}$. The AUG data at $I_P = 1$ MA contains fewer data points from 4 separate discharges and a smaller scan of $n_{e,sep}$ (factor x1.5) but does have a wider scan of $P_{div,outer}$ (factor x2.5). Finally, there is one datapoint at $I_P = 1.2$ MA from one discharge since operation at this higher current on AUG is less common.

In this analysis, the data from AUG and JET are not combined in the least squares regression because the systematic uncertainties on the measurement prevent a meaningful comparison of the data between devices. On AUG, the least squares regression is carried out firstly using the data at constant $I_P = 0.8$ MA and then again including data from all three I_P levels (allowing I_P^x as an additional free parameter). The regression using data from all three I_P scenarios is run once with c_N evaluated with a constant ΔL and again using an I_P dependent ΔL, as discussed in section 3.3. The results of the three regressions on AUG, respectively, are as follows:

$$c_N = 21.9 P_{div,outer}^{1.24\pm0.45} n_{e,sep}^{-2.71\pm0.41} \tag{3}$$

$$c_N = 28.22 P_{div,outer}^{1.19\pm0.32} n_{e,sep}^{-2.77\pm0.36} I_P^{0.69\pm0.70} \tag{4}$$

$$c_N = 28.23 P_{div,outer}^{1.19\pm0.32} n_{e,sep}^{-2.77\pm0.41} I_P^{1.69\pm0.70} \tag{5}$$

where $P_{div,outer}$ is in [MW], $n_{e,sep}$ in [10^{19} m^{-3}] and I_P in [MA]. The data consistently show a nearly linear scaling of $P_{div,outer}$ and a scaling of $n_{e,sep}$ approximately to the exponent -2.7. The I_P scaling is less certain and ranges from $0.7 - 1.7$ with a significant uncertainty. The I_P scaling could be improved by assessing the ΔL approximation with camera inversions over varying I_P.

Finally, since the data from JET are at constant $I_P = 2.5$ MA and $P_{div,outer} = 6 - 6.5$ MW, a least-squares regression of $n_{e,sep}$ was carried out on JET for the 9 separate discharges. The regression produced

$$c_N = 124.5 n_{e,sep}^{-2.43\pm0.27} \tag{6}$$

which suggests a moderately weaker dependence on $n_{e,sep}$ in comparison to the data from AUG. A comparison of the regression and measurements for AUG and JET data are shown in Fig. 8.

4.1. Detachment threshold window

To investigate the linearity of the detachment threshold window with c_N, two scenarios are assessed: first, a single discharge at $I_P = 1$ MA (AUG #35846) with three steps in injected power and a constant level of N_2 seeding; and second, a set of identical repeated discharges at $I_P = 0.8$ MA (AUG #33029–33032 [34]) with constant N_2 seeding which, due to wall-loading, results in a moderately higher c_N in each subsequent pulse. In both scenarios, Eq. 4 is used to calculate the threshold c_N. Ratios of the measured and threshold c_N are shown in Fig. 9 for the two scenarios. The series of repeat pulses reveal a more obvious trend, showing T_{div} decreasing from ≈ 15 eV to ≈ 4 eV with a near linear increase of c_N (with respect to the threshold). The single pulse, with three NBI steps, shows a similar trend for $T_{div} > 10$ eV; however, the change in the ratio is less defined for $T_{div} < 10$ eV.

5. Assessment of scaling law

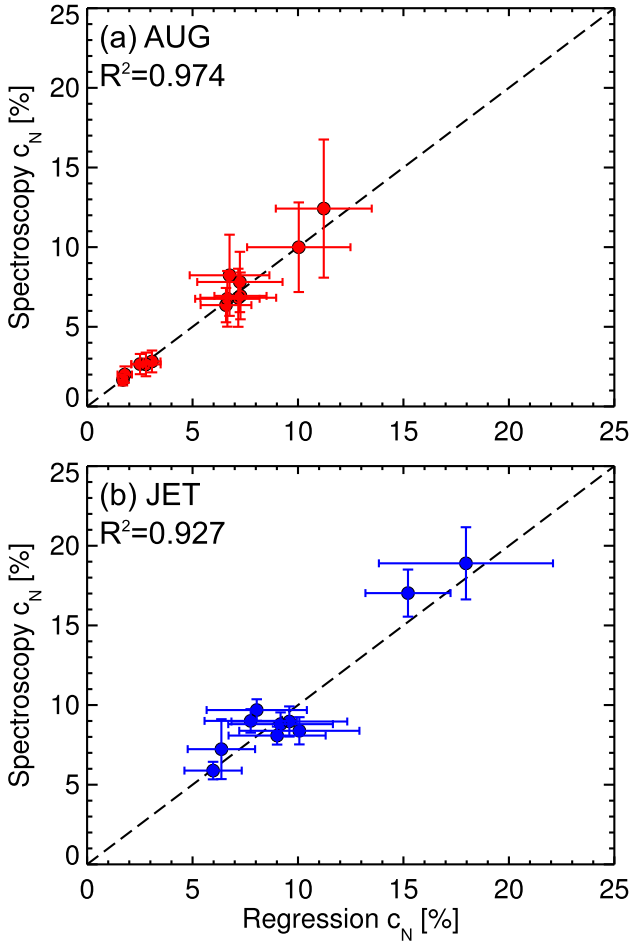The Lengyel model [16] for calculating the impurity concentration

Fig. 8. The database of c_N are shown as a function of the least-squares regression for (a) AUG using Eq. 4 and (b) JET using Eq. 6.
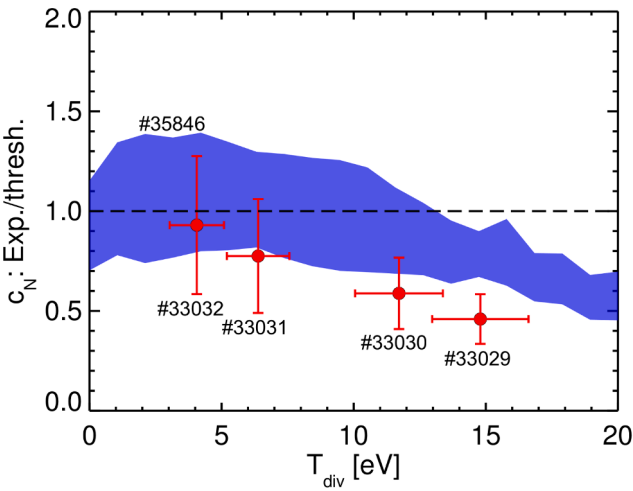

Fig. 9. The ratio of the measured and threshold c_N required for detachment is shown as a function of T_{div}. The blue shaded curve corresponds to the ratio found for a single pulse AUG #35846 measured between $t = 2 - 6$ s, while the single points correspond to data measured in a series of otherwise identical pulses.

required for detachment is given by

$$c_{N,Lengyel} = 0.5q_\parallel^2 \kappa_0^{-1} n_{e,sep}^{-2} T_{e,sep}^{-2} L_{INT}^{-1} \quad (7)$$

where $n_{e,sep}$ and $T_{e,sep}$ are the upstream separatrix density and temperature, respectively, $q_\parallel$ is the parallel heat flux proportional to $1/\lambda_q$ the exponential fall-off width of the SOL power, L_{INT} is the integral of the radiative cooling function along the SOL multiplied by $\sqrt{T_e}$, and κ_0 is the thermal conductivity. This equation was later quoted by Post (Eq. 7 [17]) and used by Reinke [19], Goldston [20] and Kallenbach [18].

The Kallenbach scaling of c_N built on a 1D model representing the region of the first e-folding length of the heat flux outside of the separatrix and included charge exchange momentum loss terms. The main result was (Eq. 9 [18])

$$c_{N,Kallenbach} = \quad 1.3 P_{div,outer} R_{maj}^{-1} f_Z^{-1} p_0^{-1}$$
$$(\lambda_{int}/0.005)^{-1} (R_{maj}/1.65)^{-0.1} \quad (8)$$

where p_0 is the divertor neutral pressure, $f_Z = 18$ is the relative radiation efficiency of N, λ_{int} is the integral power decay length relating the peak heat flux and the deposited power (approximated using $\lambda_{int} \approx \lambda_q + 1.64S$) and R_{maj} is the major radius of the magnetic axis.

Goldston's scaling uses a Heuristic Drift (HD) model [37] to calculate λ_q required for Eq. 7 with the final derivation of c_N given as (Eq. 9 excluding the term considering impurity charge and isotope mass [37])

$$c_{N,Goldston} = \quad 18.3 P_{div,outer} n_{e,sep}^{-2} I_P$$
$$a_{min}^{-3} (1 + \kappa^2)^{-1} l_{*\parallel}^{-1} \quad (9)$$

where a_{min} is the minor radius, $l_{*\parallel}$ is a dimensionless quantity to account for extended field lines, κ is the elongation, and I_P and $n_{e,sep}$ are introduced by substituting the expressions for the poloidal magnetic field $B_p = \mu_0 I_P / 2\pi a \sqrt{(1 + \kappa^2)/2}$ and $f_{GW,sep} = n_{e,sep}/n_{GW}$. The factor 18.3 is produced by normalising this result to the model by Kallenbach in Eq. 8. Reinke's scaling instead uses Eich's experimental scaling of λ_q to calculate λ_q [38] along with the Martin scaling for the L-H threshold power [39] which produces the derivation (Eq. 10 [19])

$$c_{N,Reinke} = \quad 0.014 B_T^{0.88} f_{LH}^{1.14} q_*^{0.32}$$
$$R_{maj}^{1.33} \epsilon^{0.59} n_{e,sep}^{-2} f_{GW}^{-1.18} n_{20}^{-2}$$
$$(1 + \kappa^2)^{-0.64} l_{*\parallel}^{-0.86} m_L^{-1.0} \quad (10)$$

where f_{LH} is P_{sep} over the L-H threshold power, q_* is the safety factor, f_{GW} is the volume averaged density n_{20} in units of 10^{20} m^{-3} over the Greenwald density limit, and m_L is a constant representing the gradient of L_{int} against $T_{e,sep}$.

An equivalent database of c_N to the spectroscopy measurements are calculated for each of the four scaling laws given above. The following approximations are used: λ_{int} is approximated by assuming $S \approx 2$ mm; $l_{*\parallel}$ has not been measured in this database, and has been assumed to be unity in Eq. 9 (i.e. already taken into account by the factor 18.3) and 4.33 in Eq. 10; p_0 is estimated using the scaling law derived on AUG $p_0 = (n_{e,sep}/2.65)^{3.22}$ [36] combined with the proportionality $p_0 \propto (n_{e,sep} R_{maj}^{0.5})^{3.22}$ [40] to give $p_0 = (n_{e,sep} R_{maj}^{0.5}/3.44)^{3.22}$; m_L is approximated by 0.2 according to Fig. 2 from [19] with $n_e \tau = 0.1 \times 10^{20}$ m^{-3}ms where τ is the finite residence time of the impurity ion; and finally $q_\parallel$ is calculated using Eq. 2 in [19].

The comparison of the spectrometer c_N measurement with each of the scaling law models listed above is shown in Fig. 10. In each case, the scaling law predictions are multiplied by a factor for each device to produce the best match to the experimental c_N. For the AUG data, both $c_{N,Kallenbach}$ and $c_{N,Goldston}$ are reduced by a similar factor $\approx 0.4 - 0.6$ to get the best match. This isn't surprising since $c_{N,Goldston}$ is normalised to a $c_{N,Kallenbach}$ result from an AUG discharge. The Lengyel model over-
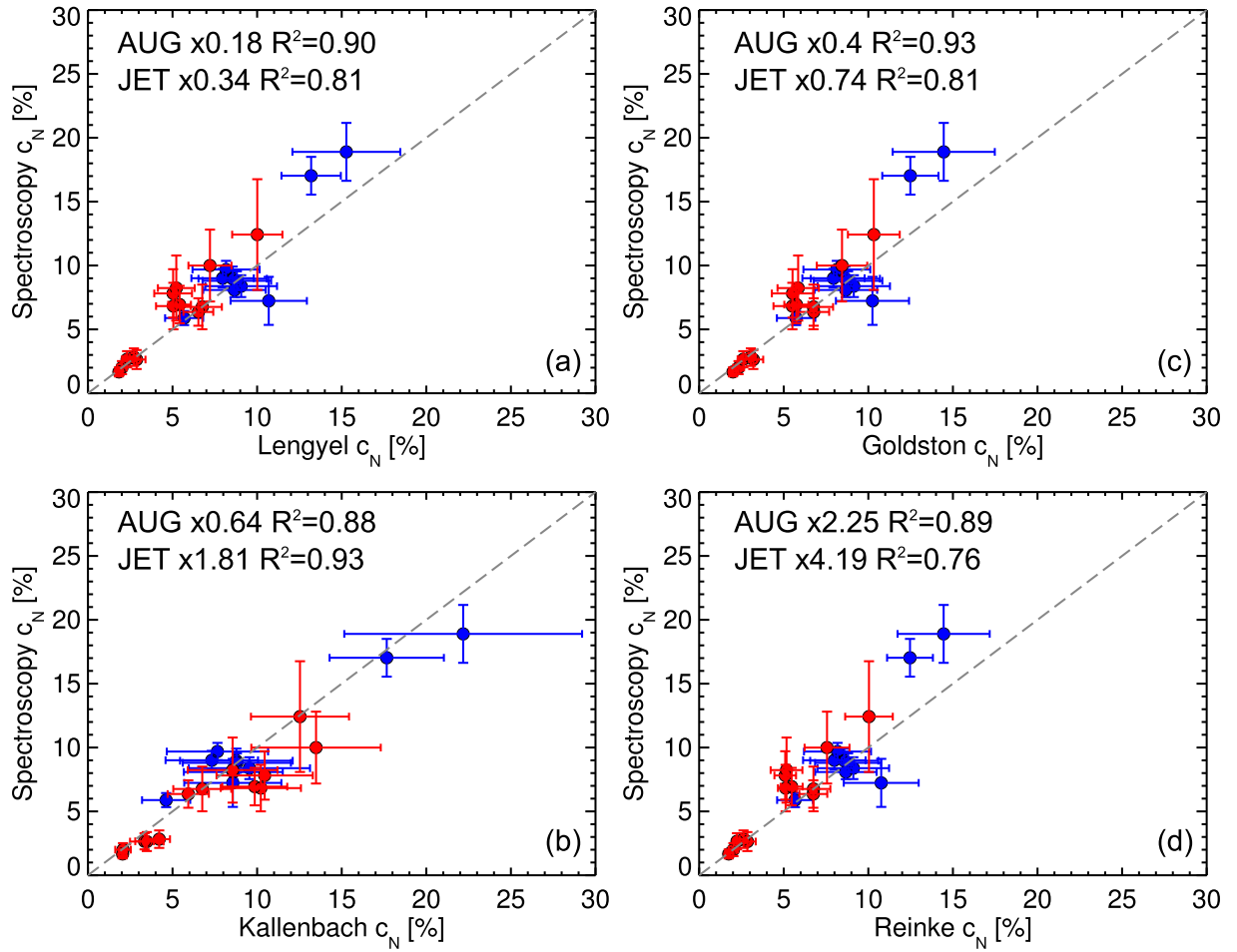
Fig. 10. The database of c_N are shown as a function of the scaling laws derived by (a) Lengyel Eq. 7 (b) Kallenbach Eq. 8 (c) Goldston Eq. 9 and (d) Reinke Eq. 10. The blue and red points indicate data from JET and AUG, respectively, with the values multiplied by the factor indicated in each subfigure.

predicts the c_N for both AUG and JET and must be reduced by a factor $\approx 0.2 - 0.3$. It has also recently been shown that the Ne concentrations taken at the detachment onset from a database of ITER baseline SOLPS-4.3 simulations are lower than the Lengyel model predictions by a factor of ≈ 0.25 [21]; a scaling factor very similar to that found in this analysis.

In general, all models predict a linear scaling with $P_{div,outer}$, with $c_{N,Reinke}$ predicting a moderately stronger dependence of $P_{div,outer}^{1.14}$. These predictions are consistent within the uncertainty of the exponent and uncertainty inferred from the experiment. The experimental c_N suggest a stronger dependence on $n_{e,sep}$, with an exponent of ≈ -2.4 on JET and ≈ -2.7 on AUG compared to an exponent of -2 predicted by all models except for $c_{N,Kallenbach}$ which predicts a stronger dependence on $n_{e,sep}$ than found in experiment ($p_0 \propto n_{e,sep}^{3.22}$).

It is worth noting that the formulations of $c_{N,Reinke}$ and $c_{N,Goldston}$ assume that λ_q can be given by an experimental scaling law and a heuristic theory, respectively, which in both cases are appropriate for low collisionality (and hence low $n_{e,sep}$) conditions. Recent experimental results show broadening of λ_q at higher collisionality [41]. The database presented in this study for both AUG and JET is within the high collisionality range where this enhanced broadening may be present. This could potentially explain the stronger dependence on $n_{e,sep}$.

6. Conclusions

A database of experimental nitrogen concentrations measured in the outer divertor on JET and AUG during N_2 seeded H-mode scenarios and averaged during periods of partial detachment have been compared

against the power flowing to the outer divertor and the separatrix density. A least-squares regression of the AUG database demonstrates that the threshold nitrogen concentration scales as $c_N \propto P_{sep}^{1.19 \pm 0.32} n_{e,sep}^{-2.77 \pm 0.36}$. The measurements from JET show approximate agreement with $c_N \propto n_{e,sep}^{-2.43 \pm 0.27}$, but does not contain a sufficient range of P_{sep} to include this parameter in the regression. The near-linear scaling with P_{sep} is consistent with predictions from the Lengyel model; however, the data indicates a moderately stronger dependence on $n_{e,sep}$. Future analysis should address the systematic uncertainties involved in the measurement, specifically concerning the approximate values used to estimate the length of the emission region. Additionally, to compare concentrations between each machine to understand the size scaling, effort should be taken to produce more consistent scenarios, reliable measurements, and include measurements from more devices. Finally, combining these new divertor concentration measurements with equivalent core charge exchange measurements will provide an approximation of the impurity enrichment.

CRediT authorship contribution statement

S.S. Henderson: Formal analysis. **M. Bernert:** Formal analysis. **C. Giroud:** Formal analysis. **D. Brida:** Formal analysis. **M. Cavedon:** Formal analysis. **P. David:** Formal analysis. **R. Dux:** Formal analysis. **J. R. Harrison:** Formal analysis. **A. Huber:** Formal analysis. **A. Kallenbach:** Formal analysis. **J. Karhunen:** Formal analysis. **B. Lomanowski:** Formal analysis. **G. Matthews:** Formal analysis. **A. Meigs:** Formal analysis. **R.A. Pitts:** Formal analysis. **F. Reimold:** Formal analysis. **M.L.**

Reinke: Formal analysis. **S. Silburn:** Formal analysis. **N. Vianello:** Formal analysis. **S. Wiesen:** Formal analysis. **M. Wischmeier:** Formal analysis.

Declaration of Competing Interest

The authors declare that they have no known competing financial interests or personal relationships that could have appeared to influence the work reported in this paper.

Acknowledgements

References

[1] R.A. Pitts, et al., Nucl. Mater. Energy 20 (2019), 100696.
[2] E.A. Lazarus, et al., Nucl. Fusion 25 (1985) 135.
[3] A. Kallenbach, et al., Nucl. Fusion 35 (1995) 1231.
[4] J. Rapp, et al., Nucl. Fusion 44 (2004) 312.
[5] J.A. Goetz, et al., Phys. Plasmas 6 (1999) 1899.
[6] C. Giroud, et al., Nucl. Fusion 53 (2013), 113025.
[7] C. Giroud, et al., Plasma Phys. Control. Fusion 57 (2015), 035004.
[8] M. Komm, et al., Nucl. Fusion 59 (2019), 106035.
[9] J.R. Harrison, et al., Plasma Phys. Control. Fusion 61 (2019), 065024.
[10] J.A. Goetz, et al., J. Nucl. Mater. 266 (1999) 354.
[11] M. Groth, et al., Nucl. Fusion 42 (2002) 591.
[12] D. Eldon, et al., Nucl. Fusion 57 (2017), 066039.
[13] A. Kallenbach, et al., Nucl. Fusion 55 (2015), 053026.
[14] M. Bernert, et al., 3rd IAEA Technical Meeting on Divertor Concepts, Vienna (Austria) (2019).
[15] F. Reimold, et al., J. Nucl. Mater. 463 (2015) 128.
[16] L.L. Lengyel, IPP Report–1/191 (1981).
[17] D. Post, N. Putvinskaya, F.W. Perkins, W. Nevins, J. Nucl. Mater. 220–222 (1995) 1014.
[18] A. Kallenbach, et al., Plasma Phys. Control. Fusion 58 (2016), 045013.
[19] M.L. Reinke, Nucl. Fusion 57 (2017), 034004.
[20] R.J. Goldston, M.L. Reinke, J.A. Schwartz, Plasma Phys. Control. Fusion 59 (2017), 055015.
[21] D. Moulton, P.C. Stangeby, X. Bonnin, R.A. Pitts, Nucl. Fusion accepted (2020).
[22] S.S. Henderson, et al., Nucl. Fusion 58 (2018), 016047.
[23] S.S. Henderson, et al., Nucl. Mater. Ener. 18 (2019) 147.
[24] A. Kallenbach, et al., Plasma Phys. Control. Fusion 52 (2010), 055002.
[25] A.E. Jaervinen, et al., J. Nucl. Mater. 463 (2015) 135.
[26] B. Lipschultz, F.I. Parra, I.H. Hutchinson, Nucl. Fusion 56 (2016), 056007.
[27] S. Wiesen et al., 1st IAEA Technical Meeting on Divertor Concepts, Vienna (Austria) (2015).
[28] S. Potzel, et al., Plasma Phys. Control. Fusion 56 (2014), 025010.
[29] A. Meigs, et al., Rev. Sci. Instrum. 81 (2010) 10E532.
[30] J. Karhunen, et al., Rev. Sci. Instrum. 90 (2019), 103504.
[31] B. Sieglin, et al., Plasma Phys. Control. Fusion 58 (2016), 055015.
[32] V. Rohde, V. Mertens, A. Scarabosio, J. Nucl. Mater. 390 (2009) 474.
[33] A. Kallenbach, et al., Nucl. Fusion 61 (2021), 016002.
[34] A. Drenik, et al., Nucl. Fusion 59 (2019), 046010.
[35] H.J. Sun, et al., Plasma Phys. Control. Fusion 59 (2017), 105010.
[36] A. Kallenbach, et al., Plasma Phys. Control. Fusion 60 (2018), 045006.
[37] R.J. Goldston, Nucl. Fusion 52 (2012), 013009.
[38] T. Eich, et al., Nucl. Fusion 53 (2013), 093031.
[39] Y.R. Martin, T. Takizuka, J. Phys, Conf. Ser. 123 (2008), 012033.
[40] A. Kallenbach, et al., Nucl. Mater. Energy 18 (2019) 166.
[41] T. Eich, et al., Nucl. Fusion 60 (2020), 056016.